RSC Advances

PAPER

View Article Online
View Journal | View Issue

Cite this: *RSC Adv.*, 2025, **15**, 35986

Hierarchical carbon-supported iron carbide derived from zinc–iron bimetallic coordination polymer as an efficient electrocatalyst for alkaline oxygen evolution

Tianlong Cao, †*[abcd] Yanfang Li,†[a] Jianguo Zhao,[ad] Qihui Jiao,[a] Wenjie Chuai,[e] Xuefei Zhang,[f] Zuopeng Li[e] and Mingjun Pang*[ad]

The development of non-precious metal catalysts with high activity, low cost and high stability represents one of the most effective strategies to tackle the prevailing challenges in the oxygen evolution reaction (OER), such as sluggish kinetics, heavy reliance on precious metals, and complex preparation protocols. Herein, a hierarchical carbon-supported iron carbide catalyst was fabricated using a zinc–iron bimetallic coordination polymer (ZnFe-CP) as the precursor, *via* a synergistic approach of self-assembly and controlled carbonization. Structural characterization, compositional analysis, and electrochemical measurements demonstrated that the zinc in ZnFe-CP not only facilitated the formation of active iron carbide phases but also enhanced the catalytic performance and kinetics toward alkaline OER. In addition, the optimized catalyst showed good OER catalytic activity in 1.0 M KOH solution, demonstrating an overpotential of 408 mV at a current density of 10 mA cm^{-2}, along with a Tafel slope of 76.1 mV dec^{-1} and a long-term stability of approximately 15 h. This work offers valuable experimental insights for the rational design and in-depth exploration of carbon-supported metal-based catalysts for energy related applications.

Received 25th July 2025
Accepted 23rd September 2025

DOI: 10.1039/d5ra05402h

rsc.li/rsc-advances

1 Introduction

The energy and ecological crisis is a major issue of global concern. To accelerate the construction of a clean, low-carbon, secure and efficient energy system, the contemporary society must cultivate renewable and clean new energy to replace human dependence on fossil fuels.[1] Hydrogen is regarded as one of the primary energy sources in the future, owing to its characteristics of zero pollution, high efficiency, abundant supply, and wide applicability.[2–4] Electrocatalytic water splitting is deemed to be among the most promising green hydrogen-production strategies. In this process, the cathode hydrogen evolution reaction (HER) and the anode oxygen evolution reaction (OER) play pivotal roles as the key determinants that significantly influence the efficiency of electrocatalytic water splitting.[5,6] More importantly, in contrast to HER, OER entails multiple proton and electron transfer procedures. Its sluggish kinetics and large overpotential exert a significant constraint on the overall efficiency of water splitting.[7,8] To date, Ru- and Ir-based precious metal materials, predominantly RuO_2 and IrO_2, continue to be the most efficient commercial catalysts in the realm of OER. They outperform Pt, Pd, and Rh owing to their lower cost and minimal overpotential at practical current densities.[9] However, several factors pose formidable barriers to the practical application of Ru- and Ir-based precious metals, which include their scarcity, exorbitant cost, as well as poor structural stability (deactivation or dissolution) under alkaline electrolytes at high potentials.[10] Therefore, the exploration and development of non-precious metal electrocatalysts, which feature high efficiency, economical cost, abundant source, facile preparation, and environmental friendliness, have emerged as a prominent research focus in the realms of chemistry and materials science.[11,12]

Transition metal-based materials, including metals, alloys, oxides, hydroxides, phosphides, carbides, nitrides, polyoxometalates, and other related compounds (with the involved metals predominantly being base metals such as Fe, Co, Ni, Cu, Mo, Zr, Ti, and W), have become a research hotspot in the field of electrocatalytic OER.[13–21] Metal–Organic Frameworks (MOFs)

[a]*Engineering Research Center of Coal-Based Ecological Carbon Sequestration Technology of the Ministry of Education, Shanxi Datong University, Datong 037009, China. E-mail: tianlong230228@163.com; pangmingjun3714@163.com*
[b]*Institute of Coal Chemistry, Chinese Academy of Sciences, Taiyuan 030001, China*
[c]*Northwest Yongxin Coating Limited Company, Lanzhou 730046, China*
[d]*Key Laboratory of Graphene Forestry Application of National Forest and Grass Administration, Shanxi Datong Universtiy, Datong 037009, China*
[e]*School of Chemistry and Chemical Engineering, Shanxi Datong University, Datong 037009, China*
[f]*Qingyuan Innovation Laboratory, Quanzhou 362801, China*
† These authors contributed equally to this work.

are composed of inorganic metal nodes and organic ligands connected by coordination and covalent bonds.[22,23] Due to the characteristics of MOF materials, such as large specific surface area, high porosity, high dispersion of metals, adjustable composition and morphology, and unique electronic structure, they are regarded as one of the most favored porous and crystalline materials in the field of catalysis.[24] They exhibit excellent electrocatalytic activity, which has attracted extensive attention from researchers. However, there are great challenges in directly using pure MOF material for OER catalysis. In the electrocatalytic process, as the catalytic reaction progresses, the metal sites in the MOF tend to undergo reconstruction, transforming into metal oxides or hydroxides.[25] This structural change causes irreversible damage to the MOF structure and diminishes the durability of the catalyst.[26] Additionally, the metal sites harbored by the MOF are occluded by organic ligands, which restricts the accessibility of reactants and gives rise to suboptimal catalytic activity. Furthermore, the inherently poor electrical conductivity of MOF poses a significant impediment to electron transfer within its structure, severely hampering its overall electrocatalytic performance.[27] In contrast, MOF-derived materials possess unique advantages, such as high dispersion of active metal, large specific area, diverse preparation techniques, abundant geometry and pore structures, and favorable selectivity towards reactants and products.[28] Especially, by pyrolyzing the MOF precursor in an inert atmosphere, MOF-derived metal/carbon structures can be obtained. During the pyrolysis process, the organic ligands can transform into a graphitized carbon skeleton with anchored sites (such as functional groups containing nitrogen and oxygen), which enhances the electron transfer ability and increases the structural stability.[29] In addition, the metal ions are reduced into nanoparticles on the surface of carbon, thereby improving the accessibility of reactants.[30] What's more, MOF-derived metal/carbon catalysts can retain the characteristic advantages of their precursors, ensuring the adjustability of the composition and structure, and the high dispersion of active sites.[31] However, for the effective dissolution of the feedstock (such as metal salts and organic ligands) and the precise control of crystal growth, the majority of synthetic approaches for MOFs primarily rely on the use of organic solvents (such as dimethylformamide, methanol, dichloromethane).[32] This reliance not only gives rise to an cumbersome preparation process (such as repeated washing, high temperature and pressure) but also amplifies the adverse effects caused by volatile organic compounds. Over time, this poses a major threat to human well-being and the ecological balance, potentially leading to health risks and environmental pollution.[33] Consequently, the effective development of structurally stable MOF-derived carbon-supported non-precious metal catalysts for OER *via* acceptable green synthesis methods remains an urgent issue that demands prompt resolution.

Iron carbide is regarded as one of the active origins for OER.[34] Nevertheless, due to the lack of suitable synthesis methods, carbon-supported iron carbide catalysts prepared *via* coordination polymer-derivations frequently coexist with iron or iron oxide particles.[35,36] This renders it arduous to unambiguously identify the catalytic active sites and reaction mechanism. In addition, the carbon-supported metal catalysts derived from zeolitic imidazolate frameworks generally present a three-dimensional block structure,[37] which substantially diminishes the utilization efficiency of metals. In contrast, two-dimensional graphene-like materials possess a thin lamellar structure, its specific surface area is much larger than that of three-dimensional materials.[38,39] Furthermore, two-dimensional catalyst material also exhibit a stronger adsorptive capacity towards reactants and a shorter diffusion pathway.[40,41] These characteristics imply that the two-dimensional catalyst can expose more active sites to the reactants, which is beneficial for augmenting the contact area between the catalyst and the reactants, thus enhancing the catalytic reaction efficiency. Currently, there are limited studies on the one-step preparation of carbon-supported homogeneous iron carbide catalysts. This trend is detrimental to the establishment of the structure-function relationship of carbon-supported iron-based catalysts, the regulation of OER kinetics, and the identification of catalytic reaction mechanism.

In consideration of the above-mentioned aspects, in this work, we have achieved the successful synthesis of novel sheet-like zinc–iron bimetallic coordination polymer precursors. The synthesis process was implemented through a self-assembly approach under ambient room temperature, employing deionized water as solvent, zinc acetate and ferric nitrate as the metallic precursors, and 2-methylimidazole as the organic coordinating ligand. After one-step controlled pyrolysis, the pre-synthesized zinc–iron bimetallic coordination polymer precursors were transformed into carbon-supported iron carbide materials. Through a series of comparative experiments and detailed structural characterizations, it was found that the pyrolyzed samples had a hierarchical structure (a composite of carbon sheets and carbon nanotubes), iron carbide was the main active source, and the introduction of zinc, coupled with the high pyrolysis temperature, facilitated the formation of homogeneous iron carbide. The optimized ZnFe(3 : 1)/C-900 catalyst (abbreviated as Fe_3C/C) exhibited good OER performances (the improvement in kinetics and increase in catalytic stability) in alkaline electrolyte.

2 Experiments

2.1 Materials

Anhydrous zinc acetate (labeled as ZA, 99.5%) was purchased from Shanghai Acmec Biochemical Technology Co., Ltd, China. 2-Methylimidazole (labeled as 2-MeIm, 95%) was purchased from Shanghai Acmec Biochemical Technology Co., Ltd, China. Anhydrous iron nitrate (labeled as IN, 98.5%) was purchased from Shanghai Acmec Biochemical Technology Co., Ltd, China. Deionized (DI) water was obtained from the water purification system produced by Shanghai Hetai Instrument Co., Ltd, China. Potassium hydroxide (labeled as PH, 98%) was purchased from Shanghai Acmec Biochemical Technology Co., Ltd, China. The above chemicals were used directly without further purification.

2.2 Preparation of Zn-CP and Zn/C sample

11.2 g of 2-MeIm was dissolved in 300 mL of DI water and stirred at room temperature (RT) for 1 h. Meanwhile, 3.74 g of anhydrous ZA was added to a separate beaker and dissolved in 100 mL of DI water with sonication assistance. Under agitation, the anhydrous ZA solution was slowly poured to the 2-MeIm solution. The mixture gradually transitioned from colorless transparent solution to white suspension within 24 h. Subsequently, the solid sample was collected by centrifuge and washed alternately with DI water to remove impurities. The final paste obtained by centrifuge was freeze-dried for 24 h to yield a dehydrated white solid powder, designed as Zn-CP (coordination polymer with zinc ion as metal node, CP: coordination polymer). Subsequently, this Zn-CP solid was transferred to a tube furnace for pyrolysis under the protection of a flowing argon atmosphere at a target temperature of 700–900 °C for 2 h, and the final sample was labeled as Zn/C-*T* (carbon supported zinc metal catalyst, *T*: 700, 800, 900).

2.3 Preparation of Fe-CP and Fe/C sample

11.2 g 2-MeIm was dissolved in 300 mL of DI water and stirred for 1 h at RT. Meanwhile, 2.73 g of IN was separately dissolved in another container containing 100 mL of DI water. Then, the IN solution was slowly added to the 2-MeIm solution under constant stirring. The state of the mixture was gradually transitioned from a clear red solution to a reddish brown suspension within 24 h. The slurry sample was obtained by centrifuge and washed with DI water to remove impurities. The reddish brown solid powder was collected by freeze-drying for 24 h, labeled as Fe-CP (coordination polymer with iron ion as metal node, CP: coordination polymer). The Fe-CP solid sample was placed in a tubular furnace and subjected to pyrolysis at 900 °C for 2 h, resulting in a product labeled as Fe/C-900 (carbon supported iron metal catalyst).

2.4 Preparation of carbon supported Fe_3C catalyst

11.2 g of 2-MeIm was dissolved in 300 mL of DI water and stirred at RT for 1 h. Meanwhile, both 3.74 g of anhydrous zinc acetate and 2.73 g of iron nitrate were simultaneously dissolved to another container containing 100 mL of DI water under sonication assistance. Subsequently, the bimetallic mixed solution was slowly added to the 2-MeIm solution. The state of the mixture gradually changed from a clear red solution to an orange suspension within 24 h. The solid component was separated by centrifuge and washed with DI water to remove impurities. The obtained orange paste was freeze-dried for 24 h to yield an orange solid powder, labeled as ZnFe(3 : 1)-CP (the number in ZnFe(3 : 1)-CP indicates that the mole ratio of zinc to iron is (3 to 1). The ZnFe(3 : 1)-CP was subsequently placed in a tube furnace and pyrolyzed under flowing argon at 900 °C for 2 h to obtain a product labeled as ZnFe(3 : 1)/C-900. In addition, to further investigate the effect of Zn/Fe feeding ratio on the reactivity of carbon-supported Fe_3C catalyst in alkaline OER, the molar ratio of Zn/Fe (including 5 : 1, 1 : 1, 1 : 3, 2 : 1) was adjusted according to the same experimental procedure as ZnFe(3 : 1)-900 without changing the organic ligand and solvent. These samples were labeled ZnFe(5 : 1)/C-900, ZnFe(1 : 1)/C-900, ZnFe(1 : 3)/C-900 and ZnFe(2 : 1)/C-900, respectively. Similarly, to evaluate the effect of pyrolysis temperature on catalyst reactivity, the preparation method was standardized for ZnFe(3 : 1)/C-900, including the solvent, metal feed ratio, organic ligand, and preparation process). The only variable adjusted was the pyrolysis temperature, which was decreased from 900 °C to 700 °C and 800 °C to prepare comparative samples. These catalysts were designated as ZnFe(3 : 1)/C-700 and ZnFe(3 : 1)/C-800. In brief, the general label for abbreviating pyrolysis samples is ZnFe(*x* : *y*)/C-*T*. Here, *x* : *y* denotes the feed molar ratio of zinc to iron used in precursor synthesis; C stands for carbon; and *T* represents the pyrolysis temperature.

2.5 Characterization

The morphology and microstructure of the samples were characterized by using a field emission scanning electron microscope (SEM, FEI QUANTA FEG250, USA) and a high-resolution transmission electron microscope (HR-TEM, Japan-JEOL-JEM 2100F) with EDAX attachment. X-ray diffraction (XRD) patterns of the sample were collected on a RIGAKU Ultima IV diffractometer from Japan using Cu Kα ($\lambda = 1.5406$ Å) at a scan rate of 15°/min and a scan range of 5° to 80°. The graphitization degree and component identification of samples were measured by a Raman spectrum (inViaReflex, UK). The element composition and valence state of the sample surface were analyzed by X-ray photoelectron spectroscopy (XPS) with a mono-chromatized micro-focused Al Kα X-ray source (Thermo SCIENTIFIC ESCALAB 250Xi, USA). The XRD, TEM and XPS data were all provided by eceshi (**https://www.eceshi.com**).

2.6 Electrochemical measurements

The electrochemical performance was studied by using a three-electrode device on an electrochemical workstation (CHI660E). The preparation process of the catalyst ink was as follows: 5 mg of powder sample was dispersed in a mixed solution of 500 μL of anhydrous ethanol and 25 μL of Nafion (5 wt%), and the homogeneous catalyst dispersion was obtained by ultrasonic oscillation for 30 min. The working electrode: 5 μL of the sample ink was dropped onto the surface of the glassy carbon electrode with a diameter of 4 mm and dried before use. The counter electrode was a platinum plate. The reference electrode was Ag/AgCl electrode. All measured potential values were calibrated to the reversible hydrogen electrode (RHE) scale according to this given equation: $E_{RHE} = E_{Ag/AgCl} + 0.059*pH + 0.198$ V. The linear sweep voltammetry (LSV) was conducted and collected in a 1.0 M KOH electrolyte, the curve test range was set to 0–1.8 V and the scanning rate was set to 5 mV s^{-1}. Prior to the test, the electrode was activated using the cyclic voltammetry (CV), and the OER performance was tested after a stable CV was obtained. The electrochemical double-layer capacitance (C_{dl}) of catalysts was determined in the non-faraday region at scanning rates of 20–100 mV s^{-1}. The calculation for electrochemical active surface area (ECSA) follows the formula: $ECSA = (S_{geo} \times C_{dl})/C_s$. In this expression, S_{geo} denotes the geometric surface

area of the working electrode, and C_s represents the specific capacitance. For the present study, the specific capacitance C_s was determined to be 0.040 mF cm^{-2}, with measurements conducted in a 1.0 M KOH electrolyte.[17,18] Electrochemical Impedance Spectroscopy (EIS) was measured at 0.182 V with a frequency range of 0.1 Hz to 100 kHz. The durability of the catalyst was carried out by chronopotentiometry, which involved continuous testing at 10 mA cm^{-2} and 50 mA cm^{-2}.

3 Results and discussion

3.1 Structure and properties of catalyst

As shown in Scheme 1, an orange sheet-like zinc–iron bimetallic coordination polymer (ZnFe-CP) was synthesized in deionized (DI) water using 2-methylimidazole (2-MeIm) as the nitrogen-containing organic ligand, alongside zinc acetate (ZA) and iron nitrate (IN) as sources of metal nodes. This synthesis was achieved through a facile combination of self-assembly, centrifugation, and freeze-drying processes conducted at room temperature (RT). Subsequently, a hierarchical carbon structure, comprising tubular and lamellar interwoven carbon, supported iron carbide catalyst, which was prepared *via* high-temperature pyrolysis under an argon atmosphere using ZnFe-CP as a precursor. Such multi-dimensional carbon structure may be conducive to the efficient dispersion of active metals and the improvement of catalytic activity in alkaline OER system.[42]

As shown in Fig. 1a and b, when the feeding ratio of zinc–iron was controlled at 3 : 1, ZnFe-CP precursor showed a uniform lamellar structure interspersed with several small fragments. However, other two contrast samples (Fe-CP and Zn-CP) showed bulk (Fig. S1a and b) and tightly stacked sheet (Fig. S1e and f). After carbonization, the morphology of resulting ZnFe(3 : 1)/C-900 partially changed from sheet-like structure to scattered bulk, and carried tubular and granular, indicating the selective collapse and transformation of CP precursor structure, and the formation of multi-dimensional structure (Fig. 1c and d), which may be owing to the carbonization of organic ligand and the volatilization of zinc.[38,43] However, the morphologies of Fe/C-900 (Fig S1c and d) and Zn/C-900 (Fig. S1g and h) after pyrolysis remained essentially identical to those of their precursors, except for only slight structural collapse, which showed that the co-existence of zinc–iron in CP was the key to the formation of multi-dimensional composite structures. The high density of voids generated by the interconnection of lamellar, bulk, and tubular structures in ZnFe(3 : 1)/C-900 can expose more catalytic sites to electrolyte, providing fast transport channels for electrons/ions, and promote O_2 desorption, which was beneficial to improve the catalytic performance of OER.[44] TEM images (Fig. 1f) and particle size distribution (Fig. S2) showed that some black particles with a diameter of 30 to 40 nm were evenly distributed in lamellar and tubular structures. HR-TEM images (Fig. 1e) revealed that distinct lattice fringes were present on the surface of the black particles in the ZnFe(3 : 1)/C-900 structure. Specifically, the lattice fringe spacings of 0.197 nm and 0.232 nm corresponded to the (112) and (121) crystal planes of Fe_3C, respectively.[45,46] This result proved that Fe_3C particle were prepared on ZnFe(3 : 1)/C-900. HAADF-STEM images (Fig. 1g) and TEM elemental mapping (Fig. 1h–m) showed that C, N, and O three elements were uniformly dispersed in the structure of ZnFe(3 : 1)/C-900. Meanwhile, the distribution area of iron element coincided with the location of black particle on ZnFe(3 : 1)/C-900, while zinc element was only sparsely dispersed on ZnFe(3 : 1)/C-900. These findings suggested that Fe_3C nanoparticles could be successfully loaded onto the N,O-codoped carbon support, and merely a negligible quantity of zinc was present in the support.

As illustrated in Fig. 2a, the XRD patterns indicated that the crystal structures of Zn-CP, Fe-CP, and ZnFe(3 : 1)-CP exhibited significant disparities. Notably, the XRD signals of Zn-CP were in full accordance with the results reported in the literature,[38] manifesting a hexagonal sheet-like ZIF structure. By contrast, the XRD pattern of Fe-CP did not show any diffraction peaks (straight line), which indicated a typical amorphous structure characteristic of an infinite coordination polymer.[47] Different from the first two samples, the XRD pattern of ZnFe(3 : 1)-CP

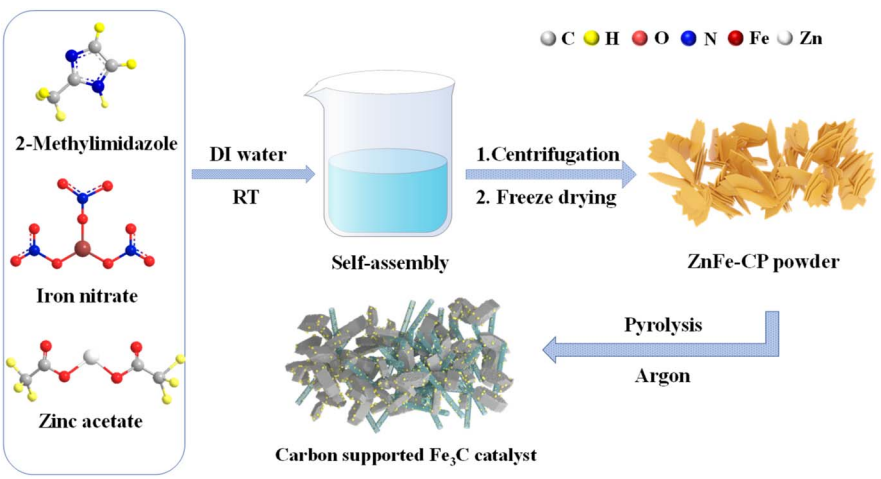

Scheme 1 Schematic illustration of the synthetic process of carbon supported Fe_3C catalyst.

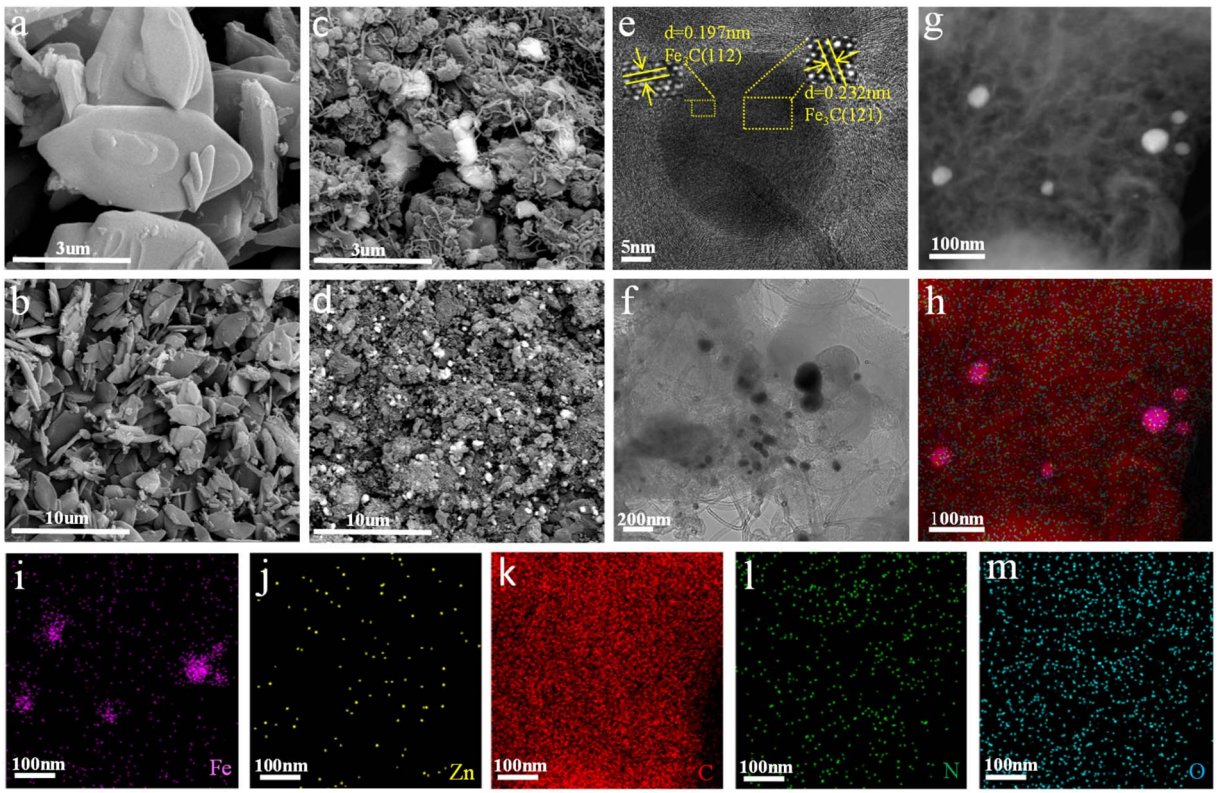

Fig. 1 SEM images of (a and b) ZnFe(3 : 1)-CP and (c and d) ZnFe(3 : 1)-900. (e and f) TEM images of ZnFe(3 : 1)/C-900. (g) HAADF-STEM image and (h–m) TEM elemental mappings of the ZnFe(3 : 1)/C-900.

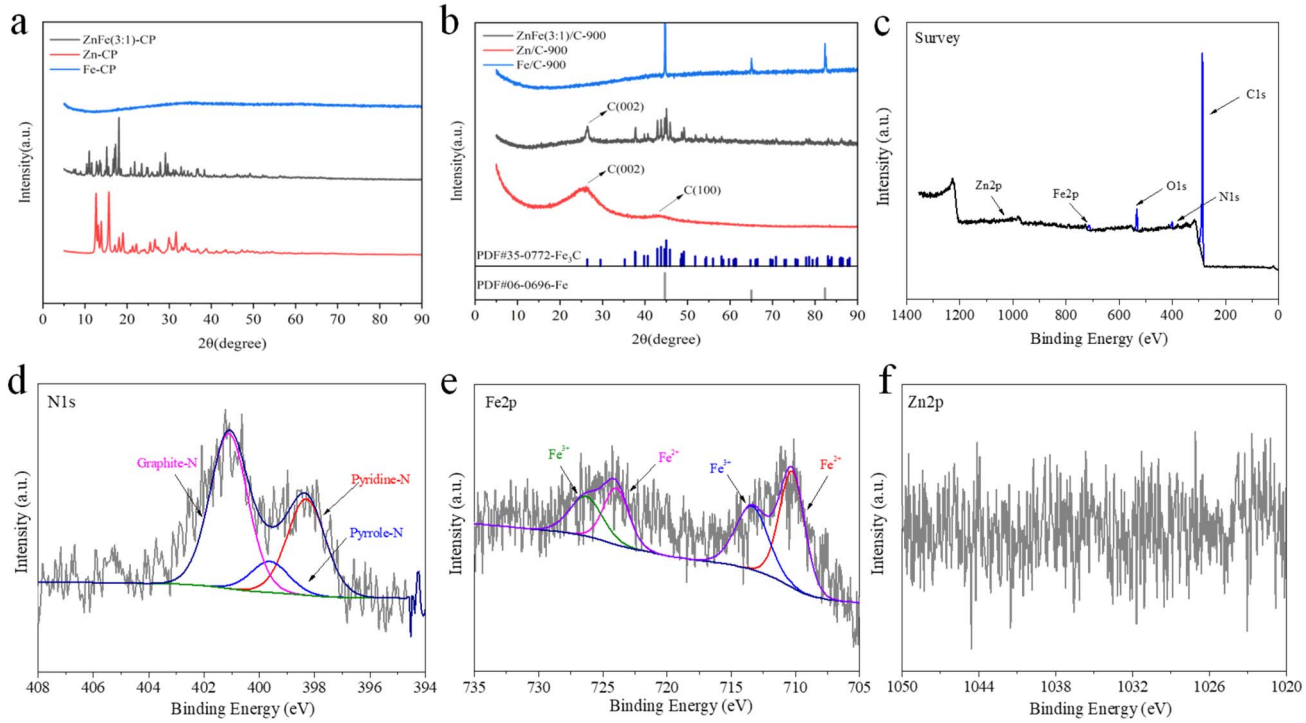

Fig. 2 (a) XRD patterns of ZnFe(3 : 1)-CP, Zn-CP and Fe-CP precursors. (b) XRD patterns of ZnFe(3 : 1)/C-900, Zn/C-900, and Fe/C-900 catalysts. (c) XPS survey of ZnFe(3 : 1)/C-900 catalyst. Deconvolution curves of (d) N1s, (e) Fe2p, and (f) Zn2p XPS fine spctra for ZnFe(3 : 1)/C-900 catalyst.

exhibited a distinct diffraction signal. This finding suggested that the coexistence of zinc and iron led to the formation of a crystalline coordination polymer with dimethylimidazole. Furthermore, the diffraction pattern of ZnFe(3 : 1)-CP was analogous to the reported XRD pattern of ZIF-8.[48] Moreover, after adjusting the ratio of zinc to iron, the XRD pattern of ZnFe-CP remained largely unchanged, as shown in Fig. S3a. Noticeable alterations in the XRD pattern were only observed when the amount of added iron significantly exceeded that of zinc (Zn : Fe = 1 : 3). The results showed that the ZnFe-CP precursors had the same crystal structure under reasonable Zn/Fe feed ratio.

After pyrolysis, the XRD pattern (Fig. 2b) of the Zn/C-900, displayed only two broad diffraction peaks centered at approximately 26° and 43° (2θ values), which were assigned to the (002) and (100) crystal planes of typical carbon, respectively.[49] This proved that zinc in the Zn/C-900 can exist in a highly dispersed form on carbon support without metal agglomeration (or particle).[38] The XRD pattern of Fe/C-900 displayed three characteristic signals (Fig. 2b) of metallic iron at about 44°, 65°, and 82° corresponding to iron standard card (PDF#06-0696), indicating the formation of iron particle on the carbon support.[50] In the XRD pattern of ZnFe(3 : 1)/C-900 (Fig. 2b), a sharp diffraction peak was observed at 26°, which can be attributed to the (002) crystal plane of the graphitized carbon.[49] At the same time, several densely arranged peaks were detected within the angular range of 35° to 60°. These peaks belonged to diffraction signals of Fe_3C phase and were consistent with the standard file (PDF#35-0772).[51] More importantly, as shown in Fig. S3b, only when the zinc to iron ratio reached 3 : 1 can iron carbide and carbon achieve the highest crystallization and the purest phase state. When the feed ratio of zinc to iron exceeded 3 : 1, the pyrolyzed sample (ZnFe(5 : 1)/C-900) mainly consisted of iron particles on carbon support (PDF#06-0696). Conversely, if the feed ratio was less than 3 : 1, the pyrolyzed samples (ZnFe(1 : 3)/C-900) mainly comprised iron oxide particles on carbon support (PDF#06-0615).[52] Apart from the optimization of the Zn–Fe metal feed ratio, the pyrolysis temperature also exerted an influence on the effective formation of iron carbide. As shown in Fig. S3c, upon a pyrolysis temperature of 700 °C, the obtained sample primarily consisted of iron/zinc/carbon compounds ($Fe_3ZnC_{0.5}$, PDF#29-0741).[53] As the pyrolysis temperature rised above 700 °C, the homogenous iron carbide phase began to form gradually (from 800 °C to 900 °C) due to the removal of zinc in $Fe_3ZnC_{0.5}$. In particular, when the temperature reached 900 °C, the crystallinity of iron carbide attained its peak value (Fig. S3c). Furthermore, while the Zn content in the ZnFe(3 : 1)/C-900 catalyst is negligible (Fig. 2f), that in the carbon-supported zinc catalyst (Zn/C-900) is substantially higher. Notably, the Zn content of a analogous catalyst (NS-ZIF8-900) can reach up to 19 wt%.[38] In combination with the detailed structural characterization findings and the aforementioned analysis, it was evident that the formation of a high-quality carbon-supported iron carbide catalyst resulted from the synergistic effect of Zn–Fe feed ratio and pyrolysis temperature, and Zn in ZnFe-CP precursor functioned merely as an intermediate species during the pyrolysis process below 700 °C, specifically forming the phase of $Fe_3ZnC_{0.5}$. As the pyrolysis temperature increased, the majority of Zn was volatilized from both carbon support and $Fe_3ZnC_{0.5}$ crystal. This should lay the foundation for the accuracy of subsequent electrochemical performance tests.

In order to further investigate the surface composition and chemical state of the ZnFe(3 : 1)/C-900, XPS analysis was conducted in this work. The signal peaks (purple line) of C, N, O, and Fe four elements can be observed in the pattern of XPS survey (Fig. 2c), which was identical with the result of elemental mappings (Fig. 1i–m). Moreover, the mass percentages of C, N, O, and Fe elements (Table S1) were 86.28%, 3.15%, 6.22%, and 3.53%, respectively. These analysis results indicated that iron can be successfully loaded onto the nitrogen- and oxygen-codoped carbon support and no undesirable substances on ZnFe(3 : 1)/C-900. Specifically, XPS fine spectrum of C1s (Fig. S4a) was deconvolved into four species, including C=O (288.9 eV), C–O (286.7 eV), C–H (285.4 eV), and sp^2-C (284.6 eV),[49] among which the content of sp^2-C was largest (41.85%) in total peak area. Fitting results and content of carbon species showed that the carbon in ZnFe(3 : 1)/C-900 manifested a certain degree of graphitization and was concomitant with several defects,[49] for instance, oxygen atom doping. This structure was conducive to the electron transfer occurring between metal and support, as well as to the anchoring of the loaded metal.[40] XPS fine spectrum of N1s (Fig. 2d) was deconvolved into three nitrogen species, graphite-N (400.8 eV), pyridine-N (398.4 eV), and pyrrole-N (399.8 eV).[34] From the viewpoint of peak area, graphite-N accounted for the largest proportion (54.96%) within the total nitrogen content. Moreover, next in line was pyridine-N (34.17%), with pyrrole-N constituting the smallest fraction (10.87%). Previous research has illustrated that N doping in carbon can enhance the adsorption of OH^- ions and accelerate the recombination of two O_{ads} moieties, thus leading to an improved OER performance.[54] Moreover, graphite-N can enhance the conductivity and electron-transfer ability, while pyridine-N provided a strong anchoring site for supported metals.[55] XPS fine spectrum of O1s (Fig. S4b) was deconvoluted into four species centered at 535.4 eV, 534.0 eV, 532.6 eV, and 531.5 eV (or 530.1 eV), which can be respectively assigned to H_2O, C–O, O=C–O, and C=O,[56] indicating abundant oxygen functional groups in carbon support. XPS fine spectrum of Fe2p (Fig. 2e) was divided into two groups of peaks, centered at 713.3 eV (726.4 eV) and 710.2 eV (724.1 eV), which were respectively attributed to the positive divalence and positive trivalence states of Fe_3C.[55] Interestingly, no signal peaks were detected in the XPS fine spectrum of Zn2p (Fig. 2f), which is likely attributed to the Zn content in the sample surface being below the detection limit (0.5 at%) of XPS. This result, when combined with the elemental mapping of zinc (Fig. 1j), indicated that only a small amount (0.16 at%, Table S1) of high dispersed zinc remained on the carbon support in ZnFe(3 : 1)-900 after pyrolysis.[38]

3.2 Performance evaluation of catalysts

The OER performance of catalysts synthesized was evaluated *via* three-electrode system. Comparison of the LSV curves (Fig. 3a)

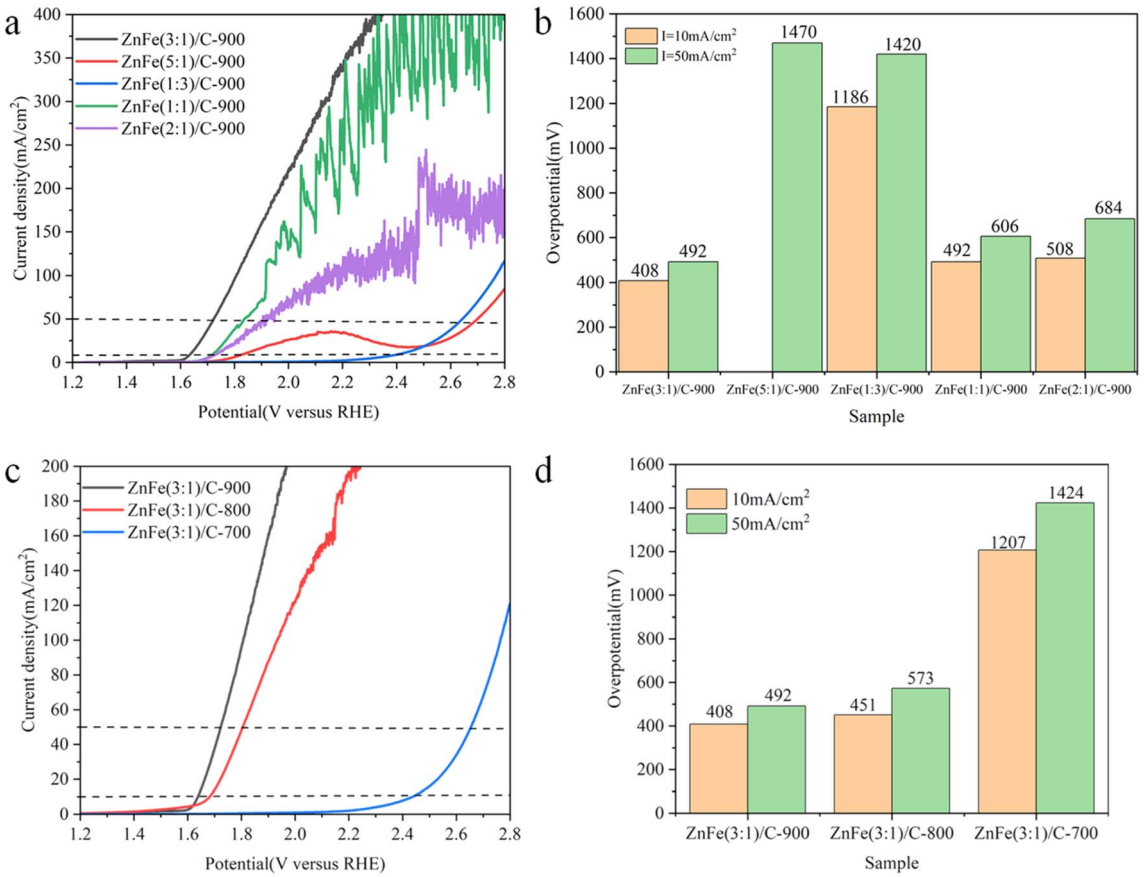

Fig. 3 Optimization of catalyst performance in alkaline (1.0 M KOH) OER system. (a) Comparison of LSV curves for catalysts with different metal feed ratios (ZnFe(3 : 1)/C-900, ZnFe(5 : 1)/C-900, ZnFe(1 : 3)/C-900, ZnFe(1 : 1)/C-900, ZnFe(2 : 1)/C-900). (b) Comparison chart of overpotential values at different current densities (10 mA cm^{-2} and 50 mA cm^{-2}) for ZnFe(3 : 1)/C-900, ZnFe(5 : 1)/C-900, ZnFe(1 : 3)/C-900, ZnFe(1 : 1)/C-900 and ZnFe(2 : 1)/C-900 catalysts. (c) Comparison of LSV curves for catalysts with different pyrolysis temperatures (ZnFe(3 : 1)/C-*X*, *X*: 700, 800, 900). (d) Comparison chart of overpotential values at different current densities (10 mA cm^{-2} and 50 mA cm^{-2}) for ZnFe(3 : 1)/C-900, ZnFe(3 : 1)/C-800 and ZnFe(1 : 3)/C-700 catalysts.

and overpotential values (Fig. 3b) of the samples pyrolyzed with different Zn–Fe feed ratios (5 : 1, 3 : 1, 2 : 1, 1 : 1, 1 : 3) revealed that the ZnFe(3 : 1)/C-900 catalyst exhibited the lowest OER overpotentials at both low current density (408 mV at 10 mA cm^{-2}) and high current density (492 mV at 50 mA cm^{-2}). Moreover, even when the current density of ZnFe(3 : 1)/C-900 was higher than 350 mA cm^{-2}, there was still no obvious fluctuation in the data shown in the LSV curve (Fig. 3a). By contrast, once the current density surpassed 75 mA cm^{-2}, the LSV curves of ZnFe(1 : 1)/C-900 (green line) and ZnFe(2 : 1)/C-900 (purple line) exhibited significant data fluctuations. In addition, a oxidation peak (red bulge) was clearly observed at approximately 2.2 V in the LSV curve of ZnFe(5 : 1)/C-900 (Fig. 3a), which is presumably attributed to the oxidation of elemental iron to iron oxides.[57,58] These aforementioned results indicated that the ZnFe(3 : 1)/C-900 exhibited the best catalytic activity and structural stability among all the control samples.[59] These superior performances might be associated with the graphitized carbon support and the pure iron carbide phase in ZnFe(3 : 1)/C-900 (Fig. S3a). Apart from the metal feed ratio, the pyrolysis temperature also exerted an influence on the performance of the catalyst, as shown in Fig. 3c and d. Only when the pyrolysis temperature reached 900 °C, the catalyst (ZnFe(3 : 1)/C-900) had the lowest overpotential (408 mV at 10 mA cm^{-2} and 492 mV at 50 mA cm^{-2}) in all samples, indicating the best OER activity. However, the catalytic performance (451 mV at 10 mA cm^{-2} and 537 mV at 50 mA cm^{-2}) of the sample pyrolyzed at 800 °C (labelled as ZnFe(3 : 1)/C-800) was slightly inferior to that of ZnFe(3 : 1)/C-900, which might be associated with the poor crystalline phase of iron carbide within its structure (Fig. S3c). Similarly, the control sample pyrolyzed at 700 °C (labelled as ZnFe(3 : 1)/C-700) showed the poorest overpotential (1207 mV at 10 mA cm^{-2} and 1424 mV at 50 mA cm^{-2}), which could be related to the transitional materials ($Fe_3ZnC_{0.5}$, Fig. S3c) in its structure.

To ascertain the active source of ZnFe(3 : 1)/C-900 in alkaline OER, performance evaluations were additionally carried out on other two reference samples with a single variable factor (the pyrolyzed samples with single metal, Zn/C-900 and Fe/C-900) under identical reaction circumstances. A comparison of the LSV curves in Fig. 4a and b clearly showed that the overpotential values of Zn/C-900 (1254 mV at 10 mA cm^{-2} and 1691 mV at 50 mA cm^{-2}) and Fe/C-900 (1186 mV at 10 mA cm^{-2} and 1418 mV at 50 mA cm^{-2}) were significantly higher than those of ZnFe(3 :

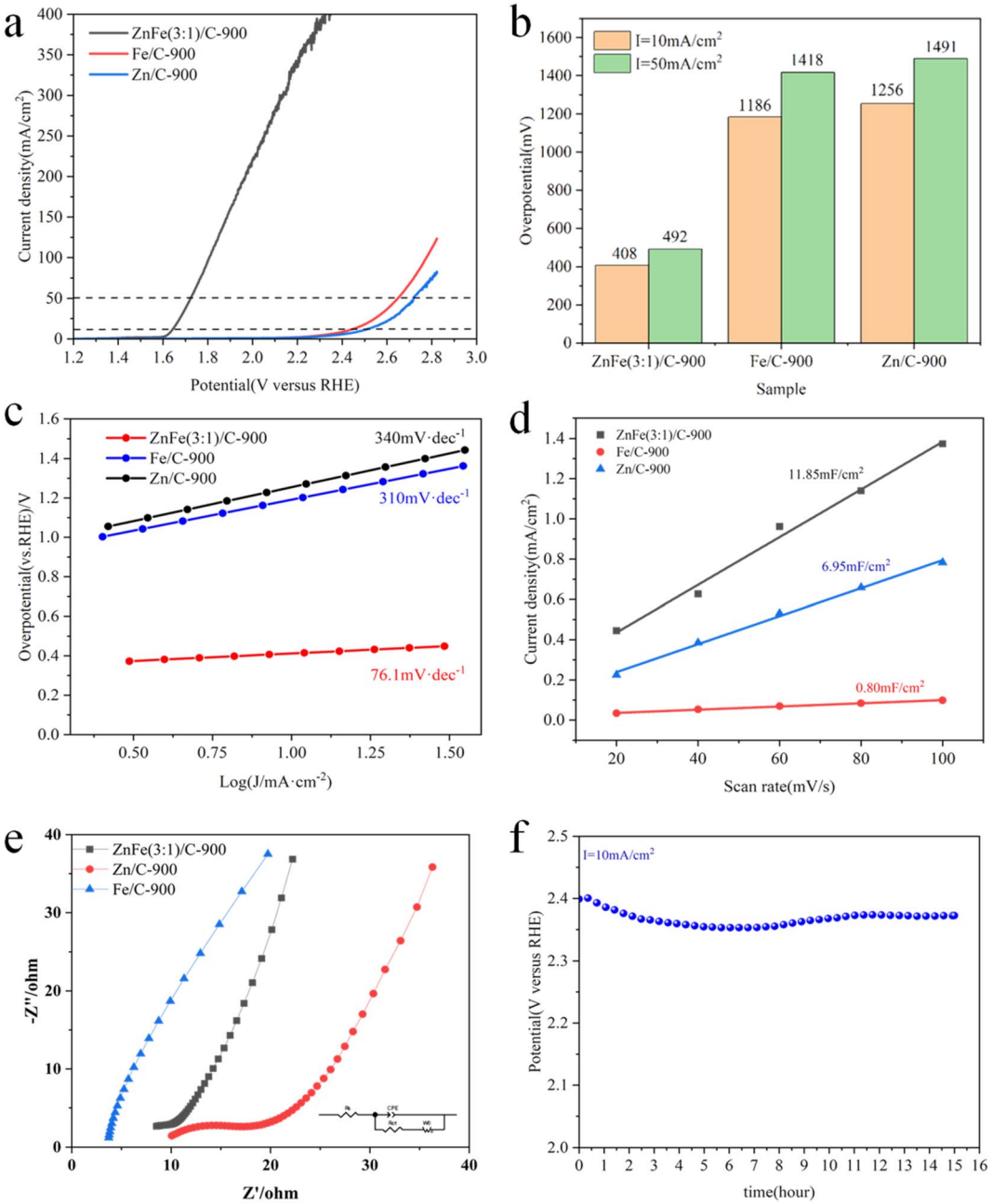

Fig. 4 Evaluation of catalyst performance in alkaline (1.0 M KOH) OER system. (a) LSV curves, (b) comparison chart of overpotential values at different current densities (10 mA cm^{-2} and 50 mA cm^{-2}), (c) Tafel plots, (d) current density plotted against the scan rate, and (e) Nyquist plots of catalysts (ZnFe(3 : 1)/C-900, Zn/C-900, and Fe/C-900). (f) Durability test of ZnFe(3 : 1)/C-900 at 10 mA cm^{-2}.

1)/C-900 (408 mV at 10 mA cm^{-2} and 492 mV at 50 mA cm^{-2}). This suggested that the OER activity of Zn/C-900 and Fe/C-900 was rather limited. This result further implied that in alkaline OER, the primary active component of the ZnFe(3 : 1)/C-900 catalyst was iron carbide supported on a hierarchical carbon structure. Furthermore, as shown in Fig. 4c, within non-faradaic region, the Tafel slope value of ZnFe(3 : 1)/C-900 was measured to be the lowest at 76.1 mV dec^{-1}, in contrast to those of Zn/C-900 (310 mV dec^{-1}) and Fe/C-900 (340 mV dec^{-1}). This distinct difference clarified that the ZnFe(3 : 1)/C-900 electrode demonstrated remarkable activity and kinetic superiority, manifested by rapid charge transfer and minimal energy loss.[60] Moreover, the Tafel slope is also a valuable tool for deducing the rate-determining steps (RDSs) of the OER process. As presented in formulas (1) to (4) in Table S3, this work employs the simplified Krasil's Chikov pathway model to investigate how the catalysts modulate the ad-/de-sorption behaviors of OH^- in electrolyte at active sites during OER.[61] As shown in Fig. 4c, the ZnFe(3 : 1)/C-900 catalyst exhibits a Tafel slope of 76.1 mV dec^{-1}, which falls within the range of 60–120 mV dec^{-1}.[61] This result indicates that the RDS of OER for ZnFe(3 : 1)/C-900 corresponds to the second elementary step, specifically the transformation of M*-OH to

M*–O^- (M: Metal) *via* the reaction M*–OH + OH^- → M*–O^- + H_2O. In contrast, the Fe/C-900 and Zn/C-900 catalysts display notably higher Tafel slopes of 310 mV dec^{-1} and 340 mV dec^{-1}, respectively. Such high Tafel slope values clarify that the RDS for these two control samples is the initial OH^- adsorption step, described by the reaction M* + OH^- → M*O–H + e^-. Collectively, these findings show that the iron carbide species play a pivotal role in enhancing the OER reaction kinetics of ZnFe(3 : 1)/C-900. Specifically, iron in iron carbide facilitates the transfer of adsorbed OH^- during the second RDS, thereby significantly boosting the overall OER electrocatalytic efficiency. The electrochemical surface area (ECSA) of contrast samples (ZnFe(3 : 1)/C-900, Fe/C-900, and Zn/C-900) was measured through the double-layer capacitance (C_{dl}), which could be calculated from the cyclic voltammetry (CV) curves acquired at scan rates ranging from 20 to 100 mV, as shown in Fig. S5. The double-layer capacitance (C_{dl}) value (Fig. 4d) of ZnFe(3 : 1)/C-900, measured at 11.85 mF cm^{-2}, surpassed those of Fe/C-900 (0.80 mF cm^{-2}) and Zn/C-900 (6.95 mF cm^{-2}). Correspondingly, the ECSA values (Fig. S6) of these catalysts, ZnFe(3 : 1)/C-900, Fe/C-900, and Zn/C-900, are 37.21 cm^2, 21.82 cm^2, and 2.51 cm^2, respectively. This result implied that ZnFe(3 : 1)/C-900 was capable of exposing a greater number of catalytic active sites and a larger accessible surface area with reactants.[62] The enhanced exposure was intricately associated with the hierarchical structure of ZnFe(3 : 1)/C-900, which was a multidimensional carbon support composed of nanosheets and nanotubes, as shown in Fig. 1c. To profoundly understand the kinetic behavior of the enhanced OER activity of ZnFe(3 : 1)/C-900, the electrochemical impedance spectroscopy (EIS) of catalysts were recorded in Fig. 4e. EIS curves of ZnFe(3 : 1)/C-900 and Zn/C-900 demonstrated a combination of a high-frequency semi-circle and a low-frequency linear tail. In contrast, the EIS curve of Fe/C-900 merely exhibited a low-frequency linear tail. Previous investigation has confirmed that the high-frequency semi-circle corresponded to the charge-transfer resistance at the electrode/electrolyte interface and the equivalent resistance of the intermediate products.[63] In contrast, the low-frequency linear tail was associated with the mass-transfer resistance of the electrolyte to active sites.[64] In comparison with Zn/C-900 and Fe/C-900, ZnFe(3 : 1)/C-900 showed a shorter semi-circular diameter and a steeper slope of linear tail. This result indicated that ZnFe(3 : 1)/C-900 possessed superior electrical conductivity, low charge-transfer resistance, and enabled the rapid electron-transfer rate, thereby enhancing the OER kinetics. After a systematic analysis of correlation between physicochemical structure of catalyst and its electrocatalytic performance, ZnFe(3 : 1)/C-900 was selected to evaluate its catalytic stability through chronopotentiometry method during continuous OER processes. As shown in Fig. 4f, S7a and b, ZnFe(3 : 1)/C-900 demonstrates outstanding stability: at a current density of 10 mA cm^{-2}, its potential is sustained continuously within the range of 2.3–2.4 V for 15 h. Moreover, following a 15 h of stability test, the catalyst's overpotential at 10 mA cm^{-2} only decreases by 84 mV relative to its pre-test value. Furthermore, the catalyst can still stably maintain a potential of 2.6 V to 2.8 V for over 11 h (Fig. S8), even at a elevanted current density of 50 mA cm^{-2}. Notably, there was no significant decline in electrode activity during this period, indicating high catalytic stability. To evaluate the catalytic stability of the catalyst in a more comprehensive manner, the structural features of the catalyst post-reaction were also characterized. As shown in Fig. S9, following a consecutive stability test for 15 h conducted at a current density of 10 mA cm^{-2} (Fig. 4f), the morphology of ZnFe(3 : 1)/C-900, the lattice fringe spacing of Fe_3C particle on the catalyst, and the elemental mappings of ZnFe(3 : 1)/C-900 exhibited negligible changes compared to their pre-reaction states (Fig. 1e and h–m). The only observable difference was the presence of the large-sized particles on catalyst surface, as shown in Fig. S9d. This result implies that during the prolonged OER process, a small fraction of Fe_3C particles undergoes a certain degree of agglomeration, a phenomenon that may be associated with the slight decline in the catalytic activity (Fig. S7). Moreover, XPS survey results from Table S4 and Fig. S10a revealed that the elemental contents of oxygen and iron in the post-reaction catalyst were higher than those in the pre-reaction sample, with oxygen content showing the most prominent increase. Specifically, the oxygen content of the catalyst was 10.09 at% immediately after the OER reaction and further increased to 32.66 at% after the stability test, the both values were significantly higher than the pre-reaction oxygen content of 4.93 at%. This observation indicates that as the OER duration extends, the oxygen generated during the reaction gradually adsorbs onto the catalyst surface, primarily in the form of carboxyl (–COOH) and carbonyl (C=O) groups (Fig. S10d). In contrast, the iron content increased moderately: it rose from the initial 0.8 at% (pre-reaction) to 1.98 at% post-OER, and further to 2.73 at% after the stability test. Notably, the increased iron content was dominated by trivalent iron (Fe^{3+}) (Fig. S10e), which may be correlated with the enlarged size of Fe_3C particles observed post-reaction (Fig. S9d). Additionally, as shown in the XPS spectrum of carbon (Fig. S10b), potassium (K) species were found to adsorb onto the catalyst surface with a gradual increase in content as the OER reaction time prolonged. In contrast, the types and contents of other elements – including as reflected by N1s XPS fine spectra (Fig. S10c) and Zn2p XPS fine spectra (Fig. S10f) – remained nearly unchanged. Collectively, the above results suggest that the agglomeration of metal particles in the catalyst and the enhanced oxygen adsorption capacity on the catalyst surface may be the important factors that could contribute to the slight deactivation observed during the long-term stability test. Briefly, relative to commercial RuO_2 and IrO_2, as well as prior reported the carbon-supported iron-based analogs, the activity, kinetic parameters and stability of ZnFe(3 : 1)/C-900 toward alkaline OER lies within the medium range, as detailed in Table S2.

4 Conclusion

In conclusion, a uniformly sheet-like zinc–iron bimetallic coordination polymer (ZnFe-CP) was synthesized by a combination of self-assembly and freeze drying methods. After controlled pyrolysis, the iron carbide particles with high

despersion were effectively loaded on a carbon support interwoven by carbon sheet and carbon tube due to the volatilization of zinc. Detailed structural analysis demonstrated that the formation of pure iron carbide phase was closely related to Zn/Fe metal feed ratio and pyrolysis temperature. The optimized electrocatalyst (ZnFe(3 : 1)/C-900) showed the best OER activity (the minimum overpotential) among all control samples. A series of comparative experiments indicated the iron carbide on hierarchical carbon support was mainly active origin of alkaline OER. In addition, ZnFe(3 : 1)/C-900 exhibited good kinetics parameters (such as low Tafel slope, large electrochemical specific surface area, fast electron thansfer rate) and long-term catalytic stability (about 15 h). This work not only offers valuable practical support for the efficient preparation of carbon-supported non-precious metal catalysts but also provides basic guidance for establishing the structure-function relationship in the field of electrocatalysis.

Author contributions

Tianlong Cao: Writing-review & editing, resources. Yanfang Li: Writing-original draft, formal analysis. Jianguo Zhao: Supervision. Qihui Jiao: Methodology. Wenjie Chuai: Investigation. Xuefei Zhang: Data curation, formal analysis. Zuopeng Li: Investigation. Mingjun Pang: Writing-review & editing, software.

Conflicts of interest

The authors declare that they have no conflicts of interest.

Data availability

Further, the data are available from the corresponding author on reasonable request.

The manuscript we submitted is a research article. All relevant data have been included within the manuscript and its SI Files. Supplementary information is available. See DOI: **https://doi.org/10.1039/d5ra05402h**.

Acknowledgements

This work is financially supported by the Doctoral Research Start-up Project of Shanxi Datong University of Shanxi Province of China (No. 2023-B-13), the College Students Innovation and Entrepreneurship Training Program of Education Department of Shanxi Province of China (No. 20240955), the Teaching Reform and Innovation Project of Shanxi Datong University of China (No. XJG2024232), the Graduate Education Innovation Project of Shanxi Datong University of China (No. 2024SJCX51), and the Applied Basic Research Project of Datong City of Shanxi Datong University of China (No. 2024065).

References

1 C. L. Hu, L. Zhang and J. L. Gong, Recent progress made in the mechanism comprehension and design of electrocatalysts for alkaline water splitting, *Energy Environ. Sci.*, 2019, **12**, 2620.
2 Y. Wang, M. Wang, Y. Yang, D. Kong, C. Meng, D. Zhang, H. Hu and M. Wu, Potential technology for seawater electrolysis: Anion-exchange membrane water electrolysis, *Chem Catal.*, 2023, **3**, 100643.
3 J. F. He, Y. Tong, Z. Wang, G. R. Zhou, X. H. Ren, J. Y. Zhu, N. Zhang, L. Chen and P. Z. Chen, Oxygenate-induced structural evolution of high-entropy electrocatalysts for multifunctional alcohol electrooxidation integrated with hydrogen production, *Proc. Natl. Acad. Sci. U. S. A.*, 2024, **121**, e2405846121.
4 G. R. Zhou, N. Zhang, Z. H. Huang, J. F. He, J. Y. Zhu, X. H. Ren, Y. Tong, H. G. Wang and P. Z. Chen, Efficient paired electrolysis of glycerol upgrading with hydrogen fuel over heterostructured Fe-$Co_2Mo_3O_8$@Co electrocatalyst, *Chem. Eng. J.*, 2025, **503**, 158619.
5 D. Wang, Y. Chen, L. Fan, T. Xiao, T. Meng, Z. Xing and X. Yang, Bulk and surface dual modification of nickel-cobalt spinel with ruthenium toward highly efficient overall water splitting, *Appl. Catal., B*, 2022, **305**, 121081.
6 X. Zhu, L. Y. Chen, Y. G. Liu and Z. H. Tang, Atomically precise Au nanoclusters for electrochemical hydrogen evolution catalysis: Progress and perspectives, *Polyoxometalates*, 2023, **2**, 9140031.
7 W. Hua, Y. Y. Li, H. H. Sun and J. G. Wang, Synergistic reconstruction of defect-enriched NiFe-LDH hierarchical structures toward large-current and stable oxygen evolution reaction, *ACS Appl. Mater. Interfaces*, 2025, **17**, 1319745–1319753.
8 X. H. Ren, C. Lin, G. R. Zhou, J. F. He, Y. Tong and P. Z. Chen, Pt-decorated spinel $MnCo_2O_4$ nanosheets enable ampere-level hydrazine assisted water electrolysis, *J. Colloid Interface Sci.*, 2024, **676**, 13–21.
9 Q. R. Shi, C. Z. Zhu, D. Du and Y. H. Lin, Robust noble metal-based electrocatalysts for oxygen evolution reaction, *Chem. Soc. Rev.*, 2019, **48**, 3181.
10 Z. P. Wu, X. F. Lu, S. Q. Zang and X. W. Lou, Non-noble-metal-based electrocatalysts toward the oxygen evolution reaction, *Adv. Funct. Mater.*, 2020, **30**, 1910274.
11 K. X. Zhang and R. Q. Zou, Advanced Transition Metal-Based OER Electrocatalysts: Current Status, Opportunities, and Challenges, *Small*, 2021, **17**, 2100129.
12 M. L. Pan, X. H. Cui, Q. Jing, H. M. Duan, F. P. Ouyang and R. Wu, Single-metal atoms supported on HfBO MBenes for efficient overall water splitting, *RSC Adv.*, 2025, **15**, 19079–19087.
13 Z. H. Pu, T. T. Liu, I. S. Amiinu, R. L. Cheng, P. Y. Wang, C. T. Zhang, P. X. Ji and W. H. Hu, Transition-Metal Phosphides: Activity Origin, Energy-Related Electrocatalysis Applications, and Synthetic Strategies, *Adv. Funct. Mater.*, 2020, **30**, 2004009.
14 X. H. Ren, Q. Y. Zhang, Y. Tong, G. R. Zhou, C. Lin, Y. Y. Zhao and P. Z. Chen, Nickel-copper alloying arrays realizing efficient co-electrosynthesis of adipic acid and hydrogen, *J. Energy Chem.*, 2025, **101**, 7–15.

15 Z. Q. Peng, H. Y. Li, Q. L. Zhou, T. F. Meng, K. Huang, C. D. Wang, P. Wang and Y. P. Zhao, Iron-doped XC-72 enhancing cobalt selenide for high-efficiency oxygen evolution reaction, *RSC Adv.*, 2025, **15**, 15729–15737.
16 H. F. Sun, J. Y. Xiong, X. Ha, Q. Yuan, X. Mao, L. Y. Zhu, H. Xua and X. C. Liu, Enhancing photocatalytic water splitting over nitrogen-rich $BaTaO_2N$ with Zr doping, *RSC Adv.*, 2025, **15**, 19836–19842.
17 S. Skakri, A. E. Attar, S. Benhaiba, B. Bouljoihel, A. Aaddane, A. Mouakkar, A. Raisa and M. E. Rhazi, Facile synthesis of a Ni-Cu composite reinforced with a para-phenylenediamine layer for enhanced hydrogen evolution reaction, *RSC Adv.*, 2025, **15**, 24256–24269.
18 S. Zubaid, M. Jabeen, H. Ahmad, A. U. R. Chaudhary, S. A. R. Naqvi, A. Tufail, A. U. Shah, Y. Khan and T. A. Sherazi, Ti_3C_2Tx MXene embedded with nickel-molybdenum sulfide for a high-performance hydrogen evolution reaction in alkaline media, *RSC Adv.*, 2025, **15**, 25393–25403.
19 S. S. Zhang, R. J. Liu, C. Streb and G. J. Zhang, Design and synthesis of novel polyoxometalate-based binary and ternary nanohybrids for energy conversion and storage, *Polyoxometalates*, 2023, **2**, 9140037.
20 R. A. Alsaiari, A. A. Abd-Ellah, Z. M. Anwar, S. S. Shata, M. M. Kamel and N. Y. Mostafa, Electrodeposition and characterization of nanostructured composite Ni-W alloys for hydrogen evolution in basic media, *RSC Adv.*, 2025, **15**, 22322–22335.
21 J. Gautam, K. Kannan, M. M. Meshesha, B. Dahal, S. Subedi, L. B. Ni, Y. G. Wei and B. L. Yang, Heterostructure of polyoxometalate/zinc-iron-oxide nanoplates as an outstanding bifunctional electrocatalyst for the hydrogen and oxygen evolution reaction, *J. Colloid Interface Sci.*, 2022, **618**, 419–430.
22 Y. An, L. L. Wang, W. Y. Jiang, X. L. Lv, G. Q. Yuan, X. X. Hang and H. Pang, Metal–organic framework-based materials for photocatalytic overall water splitting: Status and prospects, *Polyoxometalates*, 2023, **2**, 9140030.
23 I. E. Khalil, J. Fonseca, M. R. Reithofer, T. Eder and J. M. Chin, Tackling orientation of metal-organic frameworks (MOFs): The quest to enhance MOF performance, *Coord. Chem. Rev.*, 2023, **481**, 215043.
24 V. Virender, V. Pandey, G. Singh, P. K. Sharma, P. Bhatia, A. A Solovev and B. Mohan, Hybrid metal-organic frameworks (MOFs) for various catalysis applications, *Top. Curr. Chem.*, 2025, **383**, 3.
25 S. Yuan, J. Peng, B. Cai, Z. Huang, A. T. Garcia-Esparza, D. Sokaras, Y. Zhang, L. Giordano, K. Akkiraju, R. Hübner, Y. Román-Leshkov and Y. Shao-Horn, Tunable metal hydroxide-organic frameworks for catalysing oxygen evolution, *Nat. Mater.*, 2022, **21**(6), 673–680.
26 J. Du and L. Sun, Metal-organic frameworks and their derivatives as electrocatalysts for the oxygen evolution reaction, *Chem. Soc. Rev.*, 2021, **50**(4), 2663–2695.
27 Y. S. Wei, M. Zhang, R. Zou and Q. Xu, Metal-Organic Framework-Based Catalysts with Single Metal Sites, *Chem. Rev.*, 2020, **120**, 12089–12174.
28 C. Fang, X. Tang and Q. Yi, Adding Fe/dicyandiamide to Co-MOF to greatly improve its ORR/OER bifunctional electrocatalytic activity, *Appl. Catal., B*, 2024, **341**, 123346.
29 R. R. Ikreedeegh, A. Hossen, A. Sherryna and M. Tahir, Recent advances on synthesis and photocatalytic applications of MOF-derived carbon materials: A review, *Coord. Chem. Rev.*, 2024, **510**, 215834.
30 J. J. Zhang, C. X. Xu, Y. J. Zhang, Y. Z. Li, B. Liu, P. P. Huo, D. Liu and J. Z. Gui, Structural and compositional analysis of MOF-derived carbon nanomaterials for the oxygen reduction reaction, *Chem. Commun.*, 2024, **60**, 2572–2590.
31 W. B. Chen, B. B. Ma and R. Q. Zou, Rational Design and Controlled Synthesis of MOF-Derived Single-Atom Catalysts, *Acc. Mater. Res.*, 2025, **6**(2), 210–220.
32 M. El-Sayed and D. Q. Yuan, Waste to MOFs: sustainable linker, metal, and solvent sources for value-added MOF synthesis and applications, *Green Chem.*, 2020, **22**, 4082–4104.
33 A. Obeidli, H. F. Ben Salah, M. A. Murisi and R. Sabouni, Recent advancements in MOFs synthesis and their green applications, *Int. J. Hydrogen Energy*, 2022, **47**, 2567–2593.
34 S. Abbas, A. Ma, D. Seo, H. Jung, Y. Lim, A. Mehmood and K. Nam, Synthesis of Fe_3C@C core-shell catalysts with controlled shell composition for robust oxygen evolution reaction, *Appl. Surf. Sci.*, 2021, **551**, 149445.
35 G. P. Yang, T. X. Yang, Z. G. Wang, K. Wang, M. M. Zhang, P. D. Lund and S. Yun, Targeted doping induces interfacial orientation for constructing surface-functionalized Schottky junctions to coordinate redox reactions in water electrolysis, *Adv. Powder Mater.*, 2024, **3**, 100224.
36 A. Dymerska, K. Wenelska, A. Zinnatullin, R. Zairov and E. Mijowska, Electroactive heterojunctions of iron-based compounds in oxygen evolution reaction-insight into synergy and mechanism, *Electrochim. Acta*, 2024, **482**, 144005.
37 Y. Yuan, X. X. Li, X. Sun, Y. Y. Sun, M. Yang, B. Liu, D. G. Yang, H. M. Li and Y. J. Liu, Recent advances in functionalizing ZIFs and their derived carbon materials towards electrocatalytic water splitting, *Nano Energy*, 2025, **136**, 110727.
38 T. L. Cao, X. Y. Dai, Y. Fu and W. Qi, Coordination polymer-derived non-precious metal catalyst for propane dehydrogenation: Highly dispersed zinc anchored on N-doped carbon, *Appl. Surf. Sci.*, 2023, **607**, 155055.
39 B. B. Huang, Y. C. Liu and Z. L. Xie, Two dimensional nanocarbons from biomass and biological molecules: Synthetic strategies and energy related applications, *J. Energy Chem.*, 2021, **54**, 795–814.
40 A. Kumar, S. Prabhu, W. Shin, K. Yadav, Y. Ahn, M. H. Abdellattif and B. Jeon, Prospects of non-noble metal single atoms embedded in two-dimensional (2D) carbon and non-carbon-based structures in electrocatalytic applications, *Coord. Chem. Rev.*, 2022, **467**, 214613.
41 J. X. Wu, X. X. Cheng, Y. Tong, C. Lin, L. Chen and P. Z. Chen, Interface engineering on heterostructural nanosheets for efficient electrocatalytic paired upcycling of

waste plastics and nitrate, *ACS Catal.*, 2024, **14**, 18095–18106.

42 A. K. Rana and A. A. Hussain, Tailored perovskite oxide engineered with multi-dimensional carbon as electrocatalyst to concurrently improve the OER activity and electrochemical stability, *J. Mater. Sci.*, 2024, **59**, 17128–17144.

43 O. Podyacheva, A. Korobova, S. Yashnik, D. Svintsitskiy, O. Stonkus, V. Sobolev and V. Parmon, Tailored synthesis of a palladium catalyst supported on nitrogen-doped carbon nanotubes for gas-phase formic acid decomposition: A strong influence of a way of nitrogen doping, *Diamond Relat. Mater.*, 2023, **134**, 109771.

44 Q. H. Sun, J. Liu, X. L. Ji, D. D. Chen, Y. Y. Guo, L. J. Mao and J. J. Qian, Metal-organic framework derived hollow nitrogen-doped carbon sphere with cobalt phosphide in carbon nanotube for efficient oxygen evolution, *J. Colloid Interface Sci.*, 2023, **652**, 1338–1346.

45 J. H. Su, X. Zhang, Z. Q. Ma, X. Y. Xu, J. Xu and Y. J. Chen, Construction of Fe_3C@N-doped graphene layers yolk-shelled nanoparticles on the graphene sheets for high-efficient electromagnetic wave absorption, *Carbon*, 2024, **229**, 119448.

46 S. C. Li, Y. L. Ke, X. F. Zhang, S. C. Wu and Z. L. Xie, Iron carbide nanoparticles encapsulated in guanine-derived carbon for peroxymonosulfate activation, *Sep. Purif. Technol.*, 2024, **338**, 126570.

47 A. M. Spokoyny, D. Kim, A. Sumrein and C. A. Mirkin, Infinite coordination polymer nano- and microparticle structures, *Chem. Soc. Rev.*, 2009, **38**, 1218–1227.

48 G. Li, K. Sheng, Y. Lei, J. Yang, Y. L. Chen, X. W. Guo, X. G. R. Chen, B. B. Chang, T. J. Wu and X. Y. Wang, Facile synthesis of Fe_3C-dominated $Fe/Fe_3C/FeN_{0.0324}$ multiphase nanocrystals embedded in nitrogen-modified graphitized carbon as efficient pH-universal catalyst for oxygen reduction reaction and zinc-air battery, *Chem. Eng. J.*, 2023, **451**, 138823.

49 P. Q. Yan, B. S. Zhang, K. Wu, D. S. Su and W. Qi, Surface Chemistry of Nanocarbon: Characterization Strategies from the Viewpoint of Catalysis and Energy Conversion, *Carbon*, 2019, **143**, 915–936.

50 R. X. Wang, M. Z. Li, T. Liu, X. Y. Li, L. Zhou, L. Tang, C. Y. Gong, X. Gong, K. F. Yu, N. Li, W. K. Zhu and T. Chen, Encapsulating carbon-coated nano zero-valent iron particles with biomass-derived carbon aerogel for efficient uranium extraction from uranium-containing wastewater, *J. Cleaner Prod.*, 2022, **364**, 132654.

51 J. F. Li, H. C. Lan, H. J. Liu, G. Zhang, X. Q. An, R. P. Liu and J. H. Qu, Intercalation of nanosized Fe_3C in iron/carbon to construct multifunctional interface with reduction, catalysis, corrosion resistance, and immobilization capabilities, *ACS Appl. Mater. Interfaces*, 2019, **11**, 15709–15717.

52 K. Wang, D. Y. Ju, G. Y. Xu, Y. F. Wang, S. B. Chen, J. Zhang, Y. Y. Wu and W. M. Zhou, Study on electrochemical performances of composite carbon (FeO/C) materials fabricated by coal tar pitch and Fe_3O_4 particles, *Int. J. Hydrogen Energy*, 2019, **44**, 25199–25206.

53 X. B. Xie, R. L. Liu, C. Chen, D. Lan, Z. L. Chen, W. Du and G. L. Wu, Phase changes and electromagnetic wave absorption performance of XZnC (X=Fe/Co/Cu) loaded on melamine sponge hollow carbon composites, *Int. J. Miner., Metall. Mater.*, 2025, **32**, 566–577.

54 Q. F. Zhai, Y. Pan and L. M. Dai, Carbon-Based Metal-Free Electrocatalysts: Past, Present, and Future, *Acc. Mater. Res.*, 2021, **2**, 1239–1250.

55 G. F. Ma, X. Xie, K. J. Sun, H. Peng, S. Z. Cui, X. Z. Zhou, Q. T. Wang and Z. G. Lei, Facile preparation of Fe_3C decorate three-dimensional N-doped porous carbon for efficient oxygen reduction reaction, *Int. J. Hydrogen Energy*, 2020, **45**, 13272–13281.

56 T. L. Cao, X. Y. Dai, W. J. Liu, Y. Fu and W. Qi, Carbon nanotubes modified by multi-heteroatoms polymer for oxidative dehydrogenation of propane: Improvement of propene selectivity and oxidation resistance, *Carbon*, 2022, **189**, 199–209.

57 N. Hashemi and M. M. Najafpour, Nickel-induced activation of iron foam for the oxygen-evolution reaction: A multimodal study of structure and dynamics, *Inorg. Chem.*, 2025, **64**, 12824–12837.

58 C. Li, X. J. Li, Z. Y. Zhao, F. L. Li, J. Y. Xue, Z. Niu, H. W. Gu, P. Braunstein and J. P. Lang, Iron-doped NiCo-MOF hollow nanospheres for enhanced electrocatalytic oxygen evolution, *Nanoscale*, 2020, **12**, 14004–14010.

59 V. Pundir, A. Gaur, R. Kaur, Aashi and V. Bagchi, Interface-engineered Co_4N-CeF_3 heterostructure induces electronic redistribution and significantly enhances oxygen evolution at large current density, *ACS Sustain. Chem. Eng.*, 2025, **13**(9), 3491–3499.

60 Y. Jang, J. Choi, J. Moon, H. Lee and Y. Kim, Synergistic composition and surface engineering of ruthenium-cobalt hydroxide nanowires for efficient oxygen evolution catalysis, *Small*, 2025, **21**, 2409151.

61 F. H. Kong, W. W. Zhang, L. P. Sun, L. H. Huo and H. Zhao, Interface Electronic Coupling in Hierarchical FeLDH(FeCo)/$Co(OH)_2$ Arrays for Efficient Electrocatalytic Oxygen Evolution, *ChemSusChem*, 2019, **12**, 3592–3601.

62 A. Jabeen, A. Fallatah, T. Aldhafeeri, A. Alhadhrami, A. Almalki, S. Yousaf, Z. El-Bahy, M. Warsi and M. Shahid, Carbon nanotubes oriented bifunctional electrocatalyst supported on flexible material for overall water splitting, *Fuel*, 2025, **394**, 135160.

63 D. Pritzl, M. Wetjen, J. Landesfeind, S. Solchenbach and H. Gasteiger, Identifying contact resistances in high-voltage cathodes by impedance spectroscopy, *Meet. Abstr.*, 2017, **02**, 111.

64 F. Bertin, G. R. Joshi, J. Kittel, C. Sagnard, F. Ropital, M. Martinez, C. Bosch and K. Wolski, Electrochemical impedance response of a thick and porous calcium carbonate layer deposited by thermal growth on a carbon steel electrode, *Corros. Sci.*, 2024, **227**, 111778.